

RESEARCH ARTICLE | JUNE 07 2024

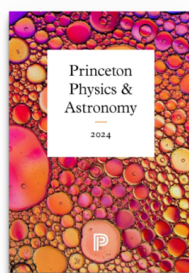
Threshold voltage mapping at the nanoscale of GaN-based high electron mobility transistor structures using hyperspectral scanning capacitance microscopy ^{EP}

Chen Chen ; Saptarsi Ghosh ; Peter De Wolf ; Zhida Liang ; Francesca Adams ; Menno J. Kappers ; David J. Wallis ; Rachel A. Oliver 

 Check for updates

Appl. Phys. Lett. 124, 232107 (2024)

<https://doi.org/10.1063/5.0203646>



Browse our new Physics and Astronomy Catalog
30% off titles with code **P326**

 PRINCETON UNIVERSITY PRESS

Threshold voltage mapping at the nanoscale of GaN-based high electron mobility transistor structures using hyperspectral scanning capacitance microscopy

Cite as: Appl. Phys. Lett. **124**, 232107 (2024); doi: [10.1063/5.0203646](https://doi.org/10.1063/5.0203646)

Submitted: 15 February 2024 · Accepted: 15 May 2024 ·

Published Online: 7 June 2024



View Online



Export Citation



CrossMark

Chen Chen,^{1,a)}  Saptarsi Ghosh,¹  Peter De Wolf,²  Zhida Liang,¹  Francesca Adams,¹  Menno J. Kappers,¹ 
David J. Wallis,^{1,3}  and Rachel A. Oliver¹ 

AFFILIATIONS

¹Department of Materials Science and Metallurgy, University of Cambridge, Cambridge CB3 0FS, United Kingdom

²Bruker Nano Surfaces, Santa Barbara, California 93117, USA

³Centre for High Frequency Engineering, University of Cardiff, Cardiff CF24 3AA, United Kingdom

^{a)} Author to whom correspondence should be addressed: cc2053@cam.ac.uk

ABSTRACT

Hyperspectral scanning capacitance microscopy (SCM) measures $dC/dV - V$ spectra at every XY location of a semiconductor sample surface area. We report its application to GaN-based high electron mobility transistor (HEMT) structures to map threshold voltage (V_{th}) at the nanoscale. The consistency between the conventional SCM data and the hyperspectral SCM data set of the same area on the HEMT surface provides evidence for the reliability of hyperspectral SCM. We developed a method to extract a map of V_{th} distribution across the surface of the HEMT structure at the nanoscale from the hyperspectral SCM data set. The map reveals that most of the fissures (i.e., enlarged pits formed at threading dislocation surface endings) on the nitride sample surface reduce local V_{th} . Other variations in V_{th} in regions free of the fissures could be a result of thickness and/or composition inhomogeneities in the $Al_xGa_{1-x}N$ barrier layer. Conventional SCM and other techniques cannot provide these detailed insights obtained through hyperspectral SCM.

© 2024 Author(s). All article content, except where otherwise noted, is licensed under a Creative Commons Attribution (CC BY) license (<https://creativecommons.org/licenses/by/4.0/>). <https://doi.org/10.1063/5.0203646>

GaN-based high electron mobility transistors (HEMTs) have a wide range of important applications, including high-power switching^{1,2} and radio frequency (RF)³ applications. Currently, the lateral dimensions of GaN-based HEMTs are being decreased down to the sub-100 nm scale to enable ultrafast performance.^{4,5} The threshold voltage (V_{th}) of a GaN-based HEMT is a measurement of the gate voltage required to turn it off. Uniformity and reproducibility of V_{th} at the nanoscale are critical in small-scale devices. For example, even with the application of reproducible processing steps, regions with different V_{th} will lead to variations in the properties of HEMTs fabricated from the same wafer. As a result, mapping V_{th} distribution of the HEMT structure at the nanoscale becomes increasingly important. However, there is no standard method for such V_{th} mapping to date. Although Schaadt *et al.*⁶ mapped lateral variations in V_{th} in a HEMT structure using scanning capacitance spectroscopy (SCS), the technique is unable to correlate V_{th} changes to specific nanoscale features. Herein,

we report the mapping of V_{th} at the nanoscale by applying hyperspectral scanning capacitance microscopy (SCM) to GaN-based HEMT structures and establish a direct correlation between nanoscale features and local V_{th} by employing a multi-microscopy⁷ approach.

SCM is an atomic force microscopy (AFM)-based technique for characterization of the local carrier density and type near the surface of semiconductors.⁸ Individual local $dC/dV - V$ spectra can be collected using SCS mode in SCM.⁹ In conventional SCM, surface topography, a dC/dV amplitude map (measured using the output, in mV , of an ultrahigh-frequency resonant capacitance sensor¹⁰), and a dC/dV phase map are acquired simultaneously so that the surface features and local electrical properties can be directly correlated. However, conventional SCM has a limitation in that the entire image is scanned at a single dc bias, which may not be the appropriate bias to deplete a HEMT sample in all locations. To investigate the impact of the features on a sample surface, the dc bias needs to be optimized.¹¹

The optimization that we have previously documented¹¹ is based on manually performing SCS measurements at certain positions on the sample surface. It is impractical to do this at each position at the nanoscale.

Hyperspectral SCM addresses this issue, giving additional insights into structure or device properties.¹² It measures local $dC/dV - V$ spectra at every XY location, producing an integrated 3D data set. Instead of employing contact mode, spectrum acquisition is embedded in the hold segment of a force curve that is part of a map captured in fast force volume (FFV) mode.¹³ As shown in Fig. 1, a conductive tip approaches the surface at each pixel in the image, then contacts the surface for a short period (the “hold segment”) while an ac bias sweeps the whole range of increasing dc biases to collect the dC/dV amplitude response, after which the tip is retracted and moves to the neighboring pixel to repeat the same process. This is in contrast to conventional SCS, which is operated with the microscope in contact mode, so large shear forces may arise during attempts to map $dC/dV - V$ spectra across the sample. This can damage the tip and lead to inconsistent performance between $dC/dV - V$ spectra, making data difficult or impossible to interpret. To reach nanoscale resolution, it is also

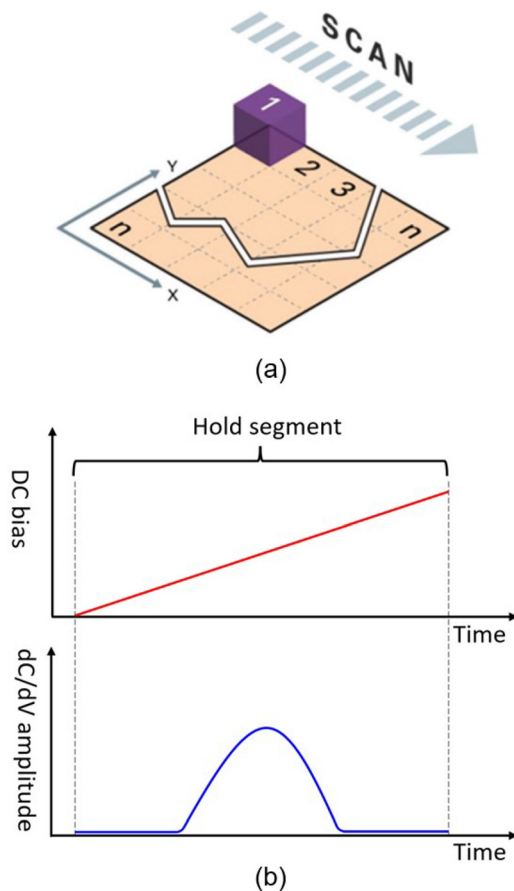


FIG. 1. The working principle of hyperspectral SCM: (a) schematic of scan pattern during the acquisition of hyperspectral SCM data.¹² Reproduced with permission from De Wolf *et al.*, *Microsc. Today* **26**(6), 18–27 (2018). Copyright 2018 Microscopy Society of America. (b) Patterns of the input dc bias (red) and the corresponding output dC/dV amplitude (blue) in the hold segment.

important that the pixel size is small enough that the depletion region achieved at the tip extends beyond the edges of the pixel. (We note here that for a blunt tip the radius of the depletion region below the tip is approximately equal to the radius of the tip–sample contact area.¹⁴) Otherwise, nanoscale features may be so small that they can be easily missed in the gap between two neighboring pixels.^{6,15}

Hyperspectral SCM has three main advantages over conventional SCM. First, both topography and a set of $dC/dV - V$ spectra are acquired simultaneously, so any of the spectra can be selected, displayed, and exported through single or multiple point(s) selection at any region of interest for further comparison and analysis. Second, the data set can generate all slices of dC/dV amplitude contrast at all the dc biases, which can highlight the evolution of the dC/dV amplitude contrast with the changing dc bias. Third, the $dC/dV - V$ spectrum at each pixel can be further analyzed to calculate the value of a specific physical parameter at that pixel, and hence a new map of the physical parameter is generated, providing more insights.

Our HEMT structure was grown on a Si (111) substrate by metal organic vapor-phase epitaxy (MOVPE). The epitaxial structure is similar to that described elsewhere¹¹ in terms of the buffer structure and the GaN channel. The barrier structure of the HEMT in this case does not include a GaN cap but consists of a 13 nm-thick AlGaIn barrier including a nominally 1 nm-thick AlN exclusion layer, as measured by high-angle annular dark-field scanning transmission electron microscopy (HAADF-STEM) (see the [supplementary material](#)). The AlN fraction of the barrier is estimated as 31% based on calibration data from AlGaIn structures grown on sapphire. Furthermore, there are three differences regarding sample fabrication and experimental setup compared to those described in Ref. 11. First, conventional metal-stack Ohmic contacts on GaN-based HEMTs require annealing at temperatures up to 850 °C, which can adversely affect material properties.¹⁶ So, here, according to an alternative method described in Ref. 16, scratches were first scribed on the sample surface and then filled with indium metal from a soldering iron to fabricate Ohmic contacts. The depth of the scratches was carefully controlled so that the indium metal directly contacted the two-dimensional electron gas (2DEG) layer near the surface but did not reach the conductive Si substrate (see the [supplementary material](#)). This avoids complications in data interpretation that may arise from applying a bias across multiple heterointerfaces in the epitaxial structure. Moreover, as the Ohmic contact is directly connected to the 2DEG, charging effects during the electrical characterizations¹⁷ are avoided. Second, the employed Adama AD-450-ASTM tip was milled before being used to perform conventional and hyperspectral SCM measurements so that the tip radius is bigger than the initial 10 nm and strong electrical signals can be achieved.¹⁴ The tip was milled *in situ* by scanning it across a $10 \times 10 \mu\text{m}^2$ area of the sample surface in contact mode multiple times, with an increased deflection setpoint and a faster scan rate compared to those used during V_{th} imaging. SCS measurement was performed after each complete scan of the area. This tip-milling procedure was stopped once the peak height of the collected $dC/dV - V$ spectra reached 200 mV. Third, when performing hyperspectral SCM measurements, the tip scanned the sample in FFV mode instead of in contact mode.

However, there is a trade-off between topographical resolution and electrical signals. A blunt conductive tip can provide strong electrical signals¹⁴ but the topographical resolution is sacrificed. Therefore, a multi-microscopy⁷ approach was employed to solve this dilemma.

The sample was first scanned in PeakForce Tapping™ mode using a sharp Bruker ScanAsyst-Air™ tip with a nominal radius of 2 nm to achieve a high-resolution topographical image. Then, we changed to a milled Adama AD-450-AS™ tip and scanned the same area to perform conventional SCM and hyperspectral SCM measurements with strong electrical signals (we note that the tip should not be milled to such an extent that it is larger than the electrical features of interest). Eventually, both high-resolution topographical images and strong conventional and hyperspectral SCM signals are achieved for the same area, allowing a direct correlation between surface features and local electrical properties. The detailed method of identifying the same area in each technique is described in the [supplementary material](#). In practice, hyperspectral SCM measurement was done first, followed by conventional SCM measurement. However, here, for easier presentation of the data, the conventional SCM data will be presented before the hyperspectral SCM data.

The hyperspectral SCM measurement was performed in DCUBE-SCM mode using a Bruker Dimension Icon Pro AFM coupled with a Bruker SCM module. It was taken at room temperature using a 90 kHz ac bias and a 990 MHz capacitance sensor. 128 pixels \times 128 pixels were collected in an $1 \times 1 \mu\text{m}^2$ area on the sample surface. The detailed method of choosing pixel size is described in the [supplementary material](#). At each pixel, a 1 V ac bias swept a dc bias range from 0 to 8.2 V. Collecting one $dC/dV - V$ spectrum at each pixel takes about 1 s. Thus, to record the hyperspectral SCM data set presented here took about 5 h.

A high-resolution topographical image of the sample surface was captured in PeakForce Tapping™ mode [Fig. 2(a)], showing nano-scale fissures (of length 60–100 nm and width 25–40 nm) that have been previously reported in similar AlGaIn/GaN heterostructures.¹⁸ However, the impact of fissures on local V_{th} has previously not been fully understood, and this topic is investigated using conventional and hyperspectral SCM in this Letter. The same area was subsequently scanned in conventional SCM mode and hyperspectral SCM mode and their topographical images are shown in Figs. 2(b) and 2(c), respectively. Matching of the broad features in the three topographic images in Fig. 2 confirms that the same area was scanned in the three different modes.

Two positions of interest are marked in the three images in Fig. 2: a measurement point on a fissure (f) and another on a non-fissure region (n) are indicated by a yellow dot and a blue dot, respectively. The test conditions for the local $dC/dV - V$ spectra measurements using SCS mode are the same for both positions, with a 1.6 V ac bias sweeping the same range of the dc biases from 0 to 8.2 V. The two resulting $dC/dV - V$ spectra are shown in Fig. 3(a). It can be seen that there is a peak shift toward negative voltage in the fissure position (f) relative to the non-fissure position (n). A shift in the peak position in the corresponding $dC/dV - V$ spectrum indicates a difference in V_{th} .¹¹ Here, it indicates that the fissure position (f) has a smaller V_{th} than the non-fissure position (n).

Based on the $dC/dV - V$ spectra in Fig. 3(a), the optimization of dc bias for mapping conventional SCM dC/dV amplitude contrast of the HEMT sample was performed subsequently. The optimum dc bias values were determined as 2.6 and 3.8 V and the corresponding dC/dV amplitude images are shown in Figs. 4(a) and 4(b). The regions with fissures appear bright in the dC/dV amplitude image at the lower dc bias [Fig. 4(a)] while dark at the higher dc bias [Fig. 4(b)]. There is contrast inversion between the two corresponding dC/dV amplitude images, which is typical for HEMT structures, as we reported previously.¹¹

The same area was scanned in hyperspectral SCM mode. The local $dC/dV - V$ spectra of the same two positions of interest (labeled as “f” and “n” in Fig. 2) are extracted and plotted in Fig. 3(b). We observed that peaks in hyperspectral SCM are consistently stronger than those in SCS, which we very tentatively attribute to differences in the tip-sample contact force in the two modes. However, the relation between the $dC/dV - V$ spectra captured on and off the fissure is consistent in both SCS and hyperspectral SCM measurements (Fig. 3). In addition, two $dC/dV - V$ amplitude slices at the fixed dc biases 2.5 and 4.6 V from the hyperspectral SCM data set are extracted and shown in Figs. 4(c) and 4(d), respectively. Changes in the appropriate dc bias ranges between the two experiments are attributed to increasing tip wear particularly during the conventional SCM optimization. However, the contrast of the dC/dV amplitude slices from the hyperspectral SCM data set is consistent with the contrast of the conventional SCM images at both lower and higher dc biases (Fig. 4).

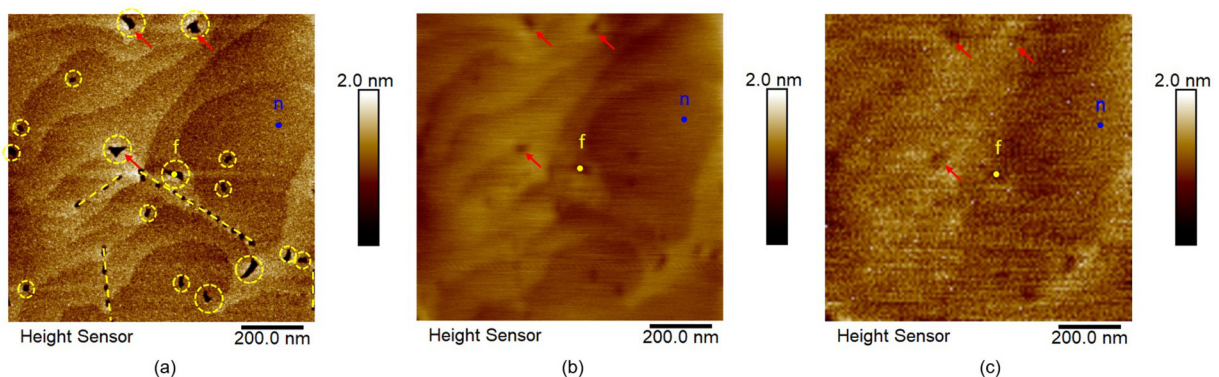


FIG. 2. Topographic images of the same area on the HEMT surface captured (a) using a sharp Bruker ScanAsyst-Air™ tip in PeakForce Tapping™ mode, (b) using a milled Adama AD-450-AS™ tip in conventional SCM mode, and (c) in hyperspectral SCM mode. The broad features marked with red arrows match each other in the three images, indicating that the same area was scanned. All the fissures are highlighted in yellow in image (a). Corresponding locations of a fissure (f) and a non-fissure region (n) in the images are indicated by a yellow dot and a blue dot, respectively.

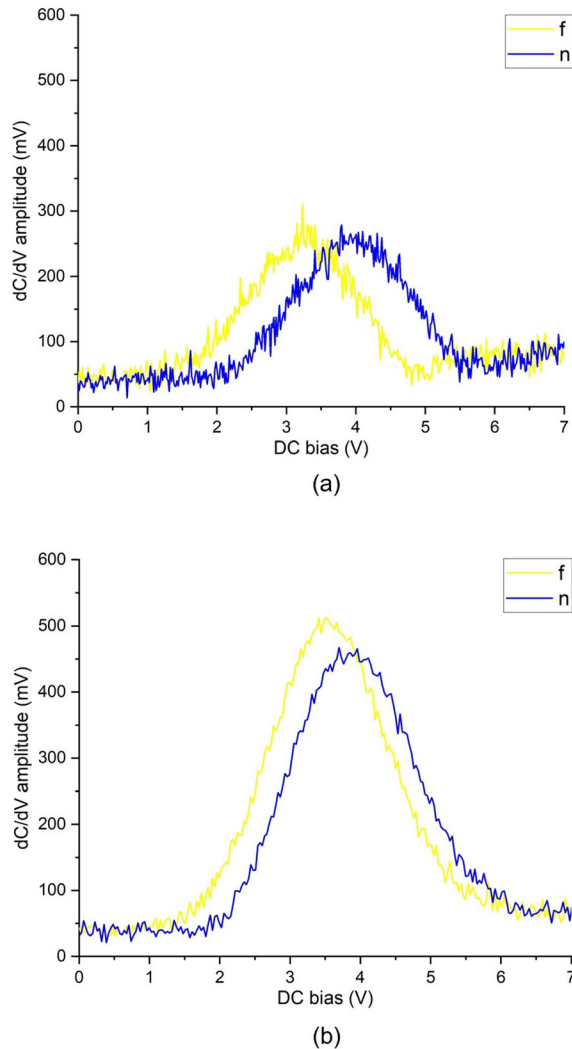


FIG. 3. Two $dC/dV - V$ spectra were captured on the fissure (f) and the non-fissure region (n) on the HEMT surface marked in Fig. 2, using (a) SCS mode and (b) hyperspectral SCM mode, respectively.

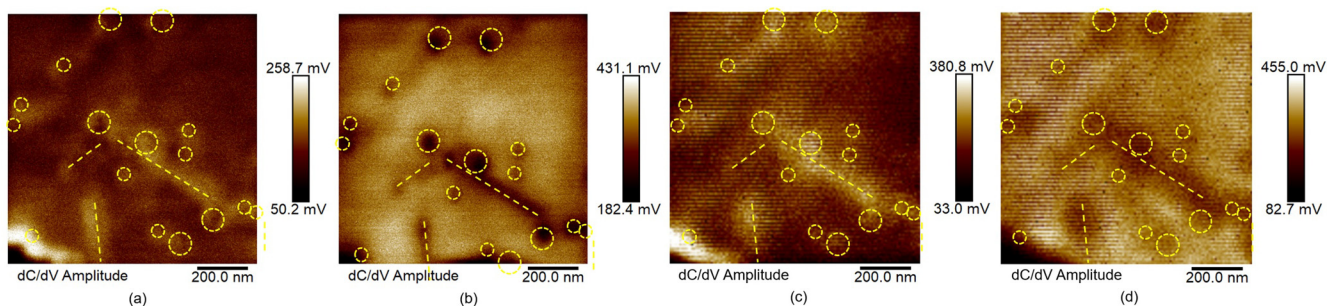


FIG. 4. dC/dV amplitude images of the same area in Fig. 2. (a) and (b) were captured in conventional SCM mode at ac bias value of 1.6 V with dc bias value of 2.6 V [on the left flank of the peaks in Fig. 3(a)] and 3.8 V [on the right flank of the peaks in Fig. 3(a)], respectively. (c) and (d) were sliced from the hyperspectral SCM data set at the dc bias value of 2.5 V [on the left flank of the peaks in Fig. 3(b)] and 4.6 V [on the right flank of the peaks in Fig. 3(b)], respectively. The position of all the fissures is highlighted in yellow.

The contrast inversion observed in these images between low and high dc bias is explained in Ref. 11. These observations suggest that the hyperspectral SCM data are reliable.

The hyperspectral SCM data set was further processed to map the V_{th} distribution in the HEMT at the nanoscale. *HyperSpy*¹⁹ was used for the relevant data analysis. First, we manually estimate the approximate peak position range, peak intensity range, and full width at half maximum (FWHM) range of the $dC/dV - V$ spectra in the data set and then input them into the program. Then, as shown in Fig. 5(a), the local $dC/dV - V$ spectrum captured in hyperspectral SCM mode is fitted to determine the peak position, which is defined as the local V_{th} value. After fitting each $dC/dV - V$ spectrum at each pixel, a map of local V_{th} distribution at the nanoscale is achieved [Fig. 5(b)]. Change in peak width and peak height from pixel to pixel is also noticed in our data, as reported previously by Schaadt *et al.*¹⁵ The origin of the change is still under investigation. Here, we focus on the peak position to generate the V_{th} map.

The position of fissures determined from Fig. 2 is highlighted in the dC/dV amplitude images (Fig. 4) and the local V_{th} map (Fig. 5) of the same area. As all the images are in nanoscale resolution, the nanoscale fissures can be directly correlated with their local dC/dV amplitude contrast and local V_{th} so that the impact of the fissures on the local electrical properties can be conveniently examined. In the nanoscale V_{th} map [Fig. 5(b)], most of the regions with fissures have a local V_{th} value lower than the averaged V_{th} value of 3.74 ± 0.16 V of the whole area. It also shows V_{th} variation in non-fissure regions (e.g., the area surrounded by red dotted lines).

The data in Fig. 2(b) show that the tip size of the milled tip is sufficiently small to allow imaging of most of the fissures. The electrical features observed in SCM [Figs. 4 and 5(b)] are larger in lateral extent than the topographic features. Hence, the tip-sample contact area is smaller than the lateral extent of the electrical feature. This is true even when the topographic fissure size is smaller than the probe. Thus, although there will be some impact of the finite tip size on the reliability of the measurement, the errors should be fairly small. The 2DEG layer is located at a depth of about 14 nm below the sample surface while the AFM-measured depth of the fissures is about 2 nm [Fig. 2(a)], so the fissures do not penetrate through the entire barrier layer. Transmission electron microscopy (TEM) measurement of the fissures also confirmed that they end within the barrier layer (data are shown in the supplementary material). Hence, it can be concluded that most of the surface fissures locally reduce the V_{th} . Fissure formation

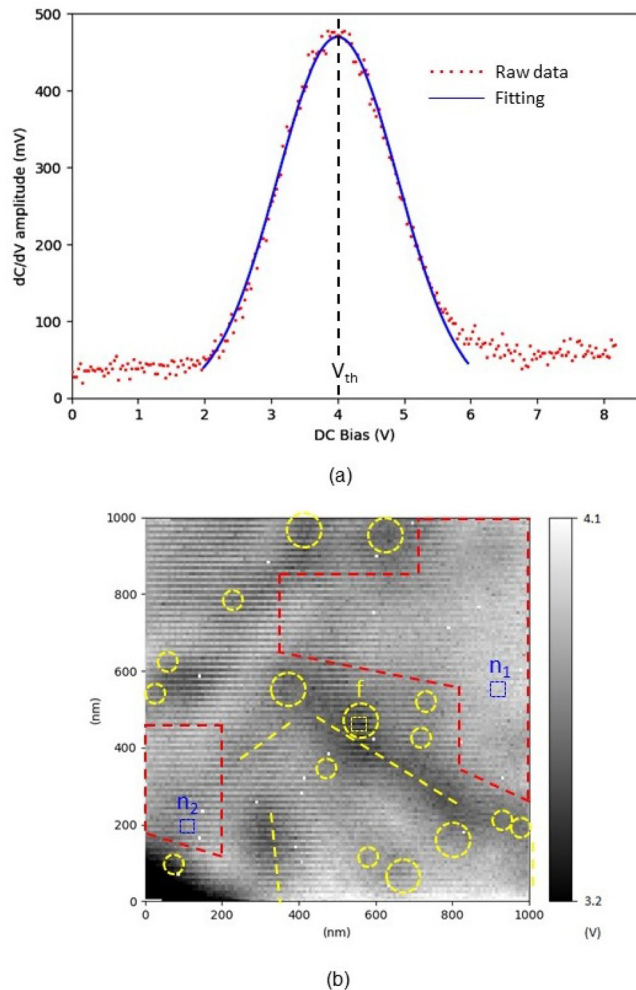


FIG. 5. (a) Determination of local V_{th} value by fitting the raw data of a local $dC/dV - V$ spectrum captured in hyperspectral SCM mode. Local V_{th} value is defined as the peak position. (b) V_{th} distribution of the same area in Fig. 2 after fitting each $dC/dV - V$ spectrum at each pixel. Fissures are highlighted in yellow. The V_{th} variation in non-fissure regions is highlighted in red. A fissure (f) and two non-fissure regions (n_1 and n_2) are labeled.

has been linked to threading dislocations (TDs).¹⁸ Typical examples are the arrays of fissures shown in Fig. 2(a). The segregation of unintentional impurities such as oxygen to the cores of dislocations in GaN may make the dislocations negatively charged.²⁰ In the case of GaN-based HEMTs, negatively charged dislocations can result in local depletion of 2DEG. Schaadt *et al.*⁶ suggested this could cause a shift in V_{th} near the dislocations. Hence, more generally, GaN-based HEMTs with TD-related defects may suffer from lower local V_{th} at the defects, which requires further investigation. Another potential reason for the lower V_{th} at the fissures could be the reduced local strain and hence reduced local 2DEG sheet carrier density resulting from strain relaxation by the fissures.

The V_{th} variation in non-fissure regions may indicate thickness or Al content inhomogeneity in the $Al_xGa_{1-x}N$ barrier layer.^{6,21,22}

Using a theoretical expression for the relation between a change in threshold voltage ΔV_{th} and a change in barrier thickness Δd for an $Al_xGa_{1-x}N$ barrier layer,⁶ we found that a thickness change of about 1 nm can result in a threshold voltage shift of about 0.31 V for our sample with a 13 nm-thick $Al_{0.31}Ga_{0.69}N$ barrier layer. We also calculated that an Al content variation $\Delta x \approx 0.06$ in the $Al_{0.31}Ga_{0.69}N$ barrier layer would yield ΔV_{th} comparable to that of a 1 nm thickness variation in our case. Therefore, based on the nanoscale V_{th} map, local thickness or Al content variation in the non-fissure regions of the $Al_{0.31}Ga_{0.69}N$ barrier layer can be estimated. The average V_{th} value for a $39 \times 39 \text{ nm}^2$ area (5 pixels \times 5 pixels) at the fissure f in Fig. 5(b) is $3.44 \pm 0.11 \text{ V}$. Similarly, the average V_{th} values for the two non-fissure regions “ n_1 ” and “ n_2 ” in Fig. 5(b) are 3.92 ± 0.02 and $3.68 \pm 0.10 \text{ V}$, respectively. The V_{th} shift between the two non-fissure regions n_1 and n_2 is about 0.24 V, which corresponds to barrier thickness variation of about 0.8 nm or Al content variation of about 0.05 (or a combination of both). The V_{th} difference between the fissure (f) and the non-fissure region (n_1) is about 0.48 V. Hence, both fissures and barrier inhomogeneities could be obstacles to a uniform and reproducible V_{th} distribution for all nanoscale HEMTs in large-scale wafers. Nanoscale HEMTs with gate contacts on or off fissured regions may therefore show different V_{th} values.

In conclusion, we applied hyperspectral SCM to GaN-based HEMT structures to map V_{th} at the nanoscale. The reliability of the hyperspectral SCM data set is illustrated by the consistency of $dC/dV - V$ spectra and dC/dV amplitude contrast between the conventional SCM data and the hyperspectral SCM data set of the same area on the HEMT surface. We have devised an approach for visualizing the V_{th} distribution in the HEMT at the nanoscale through in-depth analysis of the hyperspectral SCM data set. The V_{th} map indicates that the majority of fissures result in a decrease in the local V_{th} . Additionally, variations in V_{th} within non-fissure regions may stem from inhomogeneities in the thickness and/or Al content within the $Al_xGa_{1-x}N$ barrier layer. The inhomogeneities can be further quantified based on the local V_{th} difference in the non-fissure regions. Such detailed insights obtained by hyperspectral SCM cannot be provided by conventional SCM or other techniques. Hence, this approach can allow researchers developing growth protocols for nanoscale HEMTs to identify, which defects lead to the most substantial changes in V_{th} . This will facilitate intelligent decision-making in the optimization of epitaxial growth.

See the [supplementary material](#) for details of the HAADF-STEM image of the HEMT structure, the topographical image of a mechanically prepared scratch on the HEMT structure sample surface to which an indium contact was later soldered, the method of identifying the same area in each AFM-based technique for multi-microscopy, the methodology of choosing pixel size in hyperspectral SCM characterization, and the bright-field TEM image of a fissure in the HEMT structure sample.

C. Chen would like to thank the China Scholarship Council and the Cambridge Commonwealth, European & International Trust for a CSC Cambridge Scholarship. The authors would like to thank Dr. Gunnar Kusch for help in data analysis using HyperSpy. Materials studied here were grown using the EPSRC National Epitaxy Facility under EPSRC Grant No. EP/N017927/1. The measurements were

performed using the Royce AFM Facility under Cambridge Royce facilities Grant No. EP/P024947/1 and Sir Henry Royce Institute recurrent Grant No. EP/R00661X/1.

AUTHOR DECLARATIONS

Conflict of Interest

The authors have no conflicts to disclose.

Author Contributions

Chen Chen: Conceptualization (equal); Data curation (lead); Formal analysis (lead); Investigation (lead); Methodology (lead); Software (equal); Validation (lead); Visualization (lead); Writing – original draft (lead); Writing – review & editing (equal). **Saptarsi Ghosh:** Conceptualization (equal); Formal analysis (supporting); Investigation (supporting); Methodology (supporting); Supervision (supporting); Validation (equal); Writing – original draft (supporting); Writing – review & editing (equal). **Peter De Wolf:** Formal analysis (supporting); Investigation (supporting); Software (equal); Validation (supporting); Writing – original draft (supporting); Writing – review & editing (supporting). **Zhida Liang:** Data curation (supporting); Formal analysis (supporting); Investigation (supporting); Validation (supporting); Visualization (supporting); Writing – original draft (supporting); Writing – review & editing (supporting). **Francesca Adams:** Formal analysis (supporting); Validation (supporting); Writing – original draft (supporting); Writing – review & editing (supporting). **Menno J. Kappers:** Resources (supporting); Validation (supporting); Writing – original draft (supporting); Writing – review & editing (supporting). **David J. Wallis:** Project administration (supporting); Supervision (supporting); Validation (supporting); Writing – original draft (supporting); Writing – review & editing (supporting). **Rachel A. Oliver:** Conceptualization (lead); Formal analysis (equal); Funding acquisition (lead); Methodology (supporting); Project administration (lead); Resources (lead); Supervision (lead); Validation (equal); Writing – original draft (supporting); Writing – review & editing (equal).

DATA AVAILABILITY

The data that support the findings of this study are openly available in University of Cambridge repository at <https://doi.org/10.17863/CAM.108917>, Ref. 23.

REFERENCES

- U. K. Mishra, P. Parikh, and Y.-F. Wu, “AlGaIn/GaN HEMTs—An overview of device operation and applications,” *Proc. IEEE* **90**, 1022–1031 (2002).
- N. Ikeda, Y. Niiyama, H. Kambayashi, Y. Sato, T. Nomura, S. Kato, and S. Yoshida, “GaN power transistors on Si substrates for switching applications,” *Proc. IEEE* **98**, 1151–1161 (2010).
- I. Khalil, A. Liero, M. Rudolph, R. Lossy, and W. Heinrich, “GaN HEMT potential for low-noise highly linear RF applications,” *IEEE Microwave Wireless Compon. Lett.* **18**, 605–607 (2008).
- Y. Tang, K. Shinohara, D. Regan, A. Corrión, D. Brown, J. Wong, A. Schmitz, H. Fung, S. Kim, and M. Micovic, “Ultrahigh-speed GaN high-electron-mobility transistors with f_{Tfmax} of 454/444 GHz,” *IEEE Electron Device Lett.* **36**, 549–551 (2015).
- A. A. Fletcher and D. Nirmal, “A survey of gallium nitride HEMT for RF and high power applications,” *Superlattices Microstructures* **109**, 519–537 (2017).
- D. M. Schaadt, E. J. Miller, E. T. Yu, and J. M. Redwing, “Lateral variations in threshold voltage of an $\text{Al}_x\text{Ga}_{1-x}\text{N}/\text{GaN}$ heterostructure field-effect transistor measured by scanning capacitance spectroscopy,” *Appl. Phys. Lett.* **78**, 88–90 (2001).
- T. J. O’Hanlon, “Development of multi-microscopy techniques for the characterisation of nitride semiconductors,” Ph.D. thesis (University of Cambridge, 2019).
- R. A. Oliver, “Advances in AFM for the electrical characterization of semiconductors,” *Rep. Prog. Phys.* **71**, 076501 (2008).
- H. Edwards, R. McGlothlin, R. San Martin, E. U. M. Gribelyuk, R. Mahaffy, C. Ken Shih, R. S. List, and V. A. Ukraintsev, “Scanning capacitance microscopy: An analytical technique for pn-junction delineation in Si devices,” *Appl. Phys. Lett.* **72**, 698–700 (1998).
- J. Yang, A. Postula, and M. Bialkowski, “Circuit analysis and simulation of an ultrahigh-frequency capacitance sensor for scanning capacitance microscopy,” in *Microelectronics: Design, Technology, and Packaging* (SPIE, 2004), Vol. 5274, pp. 543–552.
- C. Chen, S. Ghosh, F. Adams, M. J. Kappers, D. J. Wallis, and R. A. Oliver, “Scanning capacitance microscopy of GaN-based high electron mobility transistor structures: A practical guide,” *Ultramicroscopy* **254**, 113833 (2023).
- P. De Wolf, Z. Huang, B. Pittenger, A. Dujardin, M. Febvre, D. Mariolle, N. Chevalier, and T. Mueller, “Functional imaging with higher-dimensional electrical data sets,” *Microsc. Today* **26**, 18–27 (2018).
- B. Pittenger and D. Yablon, “Quantitative measurements of elastic and viscoelastic properties with FASTForce volume CR,” Report No. 148 (Bruker Corporation, 2017).
- D. Schaadt and E. Yu, “Scanning capacitance spectroscopy of an $\text{Al}_x\text{Ga}_{1-x}\text{N}/\text{GaN}$ heterostructure field-effect transistor structure: Analysis of probe tip effects,” *J. Vac. Sci. Technol., B* **20**, 1671–1676 (2002).
- D. Schaadt, E. Miller, E. Yu, and J. Redwing, “Quantitative analysis of nanoscale electronic properties in an $\text{Al}_x\text{Ga}_{1-x}\text{N}/\text{GaN}$ heterostructure field-effect transistor structure,” *J. Vac. Sci. Technol., B* **19**, 1671–1674 (2001).
- C. D. Vazquez-Colon, D. C. Look, E. Heller, J. S. Cetnar, and A. A. Ayon, “Simple ohmic contact formation in HEMT structures: Application to AlGaIn/GaN,” in *Gallium Nitride Materials and Devices XIV* (SPIE, 2019), Vol. 10918, pp. 73–79.
- K. Smith, X. Dang, E. Yu, and J. Redwing, “Charging effects in AlGaIn/GaN heterostructures probed using scanning capacitance microscopy,” *J. Vac. Sci. Technol., B* **18**, 2304–2308 (2000).
- M. D. Smith, D. Thomson, V. Z. Zubialevich, H. Li, G. Naresh-Kumar, C. Trager-Cowan, and P. J. Parbrook, “Nanoscale fissure formation in $\text{Al}_x\text{Ga}_{1-x}\text{N}/\text{GaN}$ heterostructures and their influence on Ohmic contact formation,” *Phys. Status Solidi A* **214**, 1600353 (2017).
- F. de la Peña, V. T. Fauske, P. Burdet, E. Prestat, P. Jokubauskas, M. Nord, T. Ostasevicius, K. E. MacArthur, M. Sarahan, D. N. Johnstone, J. Taillon, A. Eljarrat, V. Migunov, J. Caron, T. Furnival, S. Mazzucco, T. Aarholt, M. Walls, T. Slater, F. Winkler, B. Martineau, G. Donval, R. McLeod, E. R. Hoglund, I. Alxneit, I. Hjorth, T. Henninen, L. F. Zagonel, A. Garmannslund, and A. Skorikov, *hyperspy/hyperspy v1.4.1* (Zenodo, 2018).
- D. Cherns and M. Hawkrige, “The structure and properties of dislocations in GaN,” *J. Mater. Sci.* **41**, 2685–2690 (2006).
- K. Smith, E. Yu, J. Redwing, and K. Boutros, “Scanning capacitance microscopy of AlGaIn/GaN heterostructure field-effect transistor epitaxial layer structures,” *Appl. Phys. Lett.* **75**, 2250–2252 (1999).
- K. Smith, E. Yu, J. Redwing, and K. Boutros, “Local electronic properties of AlGaIn/GaN heterostructures probed by scanning capacitance microscopy,” *J. Electron. Mater.* **29**, 274–280 (2000).
- C. Chen, S. Ghosh, P. De Wolf, Z. Liang, F. Adams, M. Kappers, D. Wallis, and R. Oliver (2024). “Research data supporting ‘Threshold voltage mapping at the nanoscale of GaN-based high electron mobility transistor structures using hyperspectral scanning capacitance microscopy,’” Apollo—University of Cambridge Repository. <https://doi.org/10.17863/CAM.108917>